Volume 8
Number 1
7 January 2020
Pages 1–178

# Journal of Materials Chemistry B

Materials for biology and medicine

rsc.li/materials-b

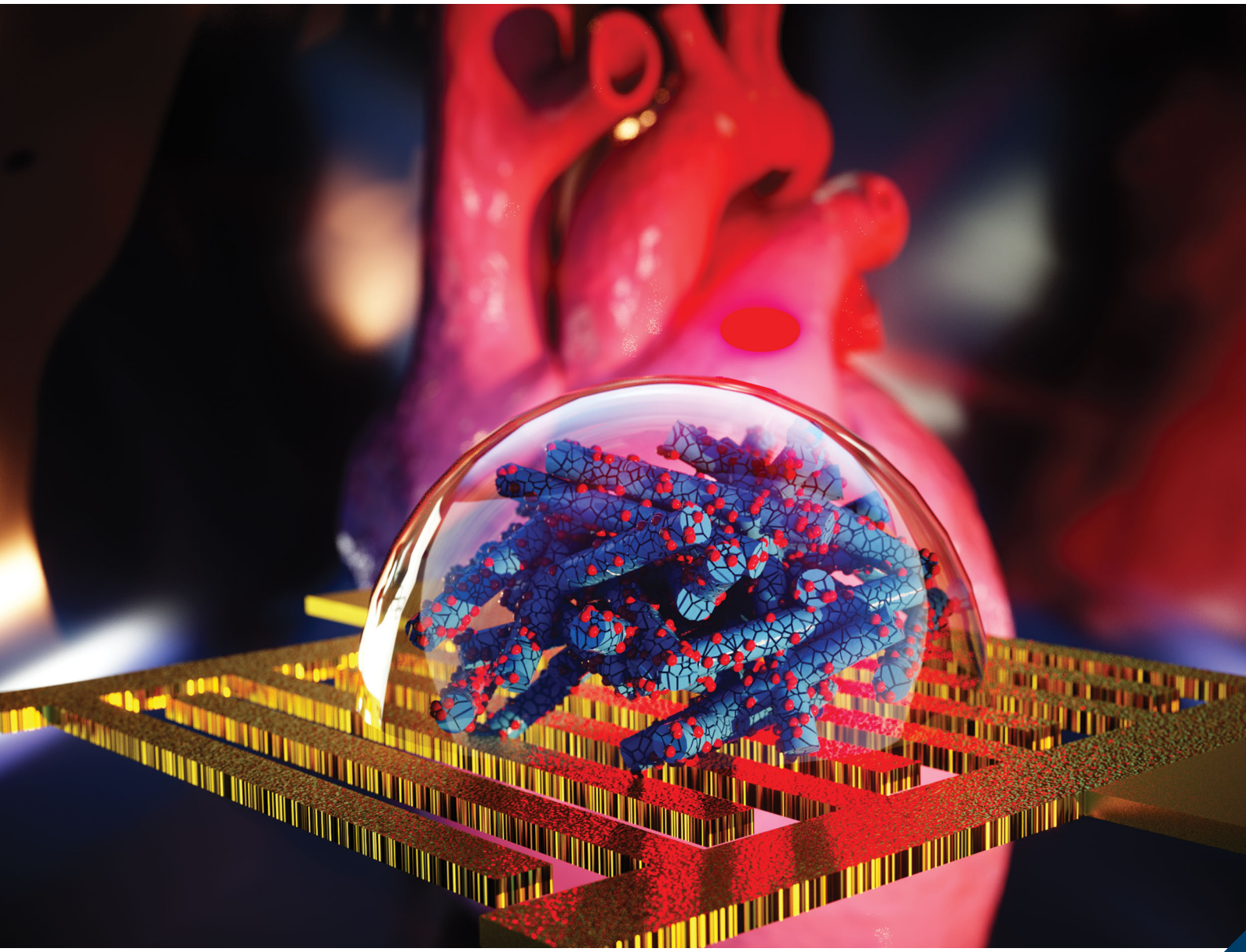

ISSN 2050-750X

ROYAL SOCIETY OF CHEMISTRY

**PAPER**

Khaled N. Salama *et al.*

A label-free aptasensor FET based on Au nanoparticle decorated $Co_3O_4$ nanorods and a SWCNT layer for detection of cardiac troponin T protein

Indexed in Medline!

Journal of Materials Chemistry B

PAPER

View Article Online
View Journal | View Issue



Cite this: J. Mater. Chem. B, 2020, 8, 18

# A label-free aptasensor FET based on Au nanoparticle decorated $Co_3O_4$ nanorods and a SWCNT layer for detection of cardiac troponin T protein

Sandeep G. Surya, †[a] Sanjit M. Majhi, †[a] Dilip K. Agarwal, [b] Abdellatif Ait Lahcen,[a] Saravanan Yuvaraja,[a] Karumbaiah N. Chappanda [ac] and Khaled N. Salama *[a]

Received 12th September 2019,
Accepted 19th November 2019

DOI: 10.1039/c9tb01989h

rsc.li/materials-b

Acute myocardial infarction (AMI) is a serious health problem that must be identified in its early stages. Considerable progress has been made in understanding the condition of AMI through ascertaining the role of biomarkers, such as myoglobin, cardiac troponin proteins (T and I), creatine kinase-MB, and fatty acid-binding protein (FABP). A field-effect transistor (FET) is an effective platform; however, innovations are required in all layers of the FET for it to become robust and highly sensitive. For the first time, we made use of the synergistic combination of noble metal nanoparticles (AuNPs) with $Co_3O_4$ for the detection of cardiac troponin T (cTnT) in a FET platform. We determined the morphology of Au-decorated $Co_3O_4$ NRs and their electronic properties by characterizing the channel layer using electron microscopies and transient measurements. Subsequently, we performed the detection of cardiac troponin T by immobilizing its complementary biotinylated DNA aptamer on the channel surface using a drop-casting method. To understand the changes in drain current caused by this interaction, we probed our SWCNT–$Co_3O_4$ NR transistor with limited gate and drain bias ($\leq$1 V), achieving a sensitivity of 0.5 $\mu A\ \mu g^{-1}\ mL^{-1}$ for the Au-decorated NRs. A 250% increase in the sensitivity and a limit of detection (LOD) of 0.1 $\mu g\ mL^{-1}$ were achieved by using this device. Finally, selectivity studies proved that this synergistic combination works well in the FET configuration for the successful detection of cTnT.

## Introduction

One of the most critical causes of heart-related deaths is acute myocardial infarction (AMI), and the highest risk of death is during the initial hours of AMI onset. Researchers are earnestly pursuing ways to detect the AMI condition with high sensitivity.[1–3] Biomarkers have been used for early diagnosis of such conditions, and an increasing amount of research is attempting to find such novel markers. Thus far, point-of-care devices embedded with biosensors are used for the detection of markers in AMI, which exclusively detect potent markers such as myoglobin,[4] fatty acid-binding protein (FABP),[5] and troponin proteins.[6] One of the most widely used biomarkers for AMI is cardiac troponin T (cTnT), the concentration of which spikes in the blood within 3–4 hours of AMI. In addition, multiple sensor configurations and approaches are implemented to identify the AMI condition. For example, immunosensors that rely on capacitive[7] and conduction[8] transduction are already in use; these require more complex electronics and are bulky in nature. By contrast, electrochemical[9] and piezoresistive cantilever[10] transduction involve complex processes and multilevel lithography steps that increase the overall cost. Thus, developing a transduction mechanism that is simple in terms of process as well as low in cost is crucial. Field-effect transistors (FETs) and chemiresistors are two other[11] alternative platforms that address the aforementioned problems of the various transduction techniques.

A sensor-element dimension reduced to the scale and size of the analyte being detected will potentially improve the sensitivity.[11] A silicon-based sensing platform with nanostructures provides an opportunity to merge the biological world with a non-biological entity to realize integrated sensors. Micro-electro-mechanical-sensors (MEMS) and nano-electromechanical-sensors (NEMS) were used in sensing biological analytes with high

[a] Sensors Lab, Advanced Membranes and Porous Materials Center, Computer, Electrical and Mathematical Science and Engineering Division, King Abdullah University of Science and Technology (KAUST), Saudi Arabia. E-mail: khaled.salama@kaust.edu.sa
[b] CRNTS, Indian Institute of Technology Bombay, Mumbai – 400076, India
[c] Department of Electrical and Electronics Engineering, Birla Institute of Technology and Science, Hyderabad 500078, India
† Equal contribution.

precision and accuracy;[12] however, although research into these sensors began three decades ago, they could not be commercialized successfully. In the complementary metal-oxide–semiconductor industry, FET devices that are miniaturized with a top-down approach are capable of delivering devices as per the scale of analytes.[13] Such transducers possess many advantageous attributes, such as excellent sensitivity and selectivity, the ability to be used for label-free detection of various analytes, and being simple in terms of fabrication and on-chip integration, all of which make them excellent candidates for point-of-care systems.[14] Various types of functional nanomaterials such as semiconductor nanoparticles,[15] carbon-based nanostructures,[16] metal chalcogenides,[17] and semiconducting metal oxides (SMOs)[18] have been reported and fabricated for FET-based biosensors. For example, Kim *et al.* reported FET biosensors based on silicon nanowires (Si-NWRs) with honeycomb nanostructures for the label-free detection of cardiac troponin I (cTnI) with high sensitivity.[19] Silva *et al.* reported using functionalized SWCNT screen-printed FET-based sensors for the detection of cTnT. Mao *et al.* demonstrated a FET-based biosensor using gold (Au) nanoparticle RGO-decorated vertically oriented graphene sheets for highly sensitive and selective protein detection.[20] Lee *et al.* presented a $MoS_2$-based label-free FET biosensor for the detection of prostate-specific antigen (PSA).[21] In addition, SMO nanomaterials have attracted tremendous attention from researchers for biosensing applications, in fields such as medical diagnosis and drug delivery. They have exhibited unique physicochemical properties with biocompatibility and interesting catalytic properties, and possess the advantages of large-scale production and cost efficiency.[22] Furthermore, SMO nanomaterials offer a high surface area and strong adsorption capability for the immobilization of biomolecules, resulting in improved electron transfer between the biomolecules and transducer electrodes, thereby enhancing the biosensing performance. Recently, various nanostructures of metal oxides (MOs) have been reported on FET-based biosensors and immunosensors. For example, Liu *et al.* demonstrated highly sensitive and rapid diagnosis of AMI biomarkers (*i.e.*, cTnT) utilizing sputter-coated $In_2O_3$ nanoribbon-based FET biosensors.[23] Moreover, Fathil *et al.* reported ZnO-based FET biosensors for cardiac troponin T. They prepared ZnO thin-film transducers using an electron beam evaporator and modified their surface with APTES and glutaraldehyde linkers to immobilize the bioreceptor antibody.[24] Similarly, in our previous work, we successfully demonstrated a sputtered ZnO FET modified with a DNA aptamer for the detection of cTnT.[25]

As is evident from the above mentioned reports, mostly n-type MOs have been employed in biosensing applications for the investigation of troponin T. Furthermore, it can be seen that progress in the design of high-performance p-type MO biosensors is still in the early stages of investigation. Therefore, investigating the biosensing behavior of p-type MOs would be interesting. Among the different p-type MOs, $Co_3O_4$ is a promising material with a relatively high isoelectric point value (approx. 8) and is an effective electrocatalytic material used in biosensing applications.[26] However, to the best of our knowledge, sensing properties for the detection of cTnT using $Co_3O_4$ nanomaterials have never been reported. We believe that the sensing performance of biosensors can be improved in various ways; for example, by incorporating foreign nanomaterials such as noble metal nanoparticles and other oxides onto the sensing element to design a composite structure, as well as by controlling the morphology of the nanomaterials.[27] Metal nanoparticles play a crucial role in immobilizing biomolecules and enhancing the response signal owing to their high surface area, excellent conductivity and high surface free energy.[28,29]

In this article, we report a chemically functionalized FET device with Au-decorated p-type $Co_3O_4$ NRs and SWCNTs as a receptor-cum-channel layer for the detection of cTnT. Specifically, the biotin–streptavidin receptor layer was immobilized on the surface of the device stack in order to enhance the sensitivity towards the target. Whereas, the nanomaterials used here and their combinations enhance the sensitivity aspect of the sensor. Noble metal nanoparticle–metal oxide-based composite materials have been gaining considerable attention because they show novel functionality caused by the synergistic effect compared with their individual components. Among the various noble metal nanoparticles, Au nanoparticles have been the most frequently used until now for applications such as catalysis,[30] gas sensing,[31] and biosensing.[32] P-type semiconducting $Co_3O_4$ NRs were used for the first time in the sensing of cTnT to assess the AMI condition. Our analytical sensor is a microelectronic-inspired device with a combination of biologically sensitive and transduction elements. SWCNTs have been widely used as a channel material in transistors and are p-type semiconductors. They play a crucial role in the basic device functioning of transistors. On the other hand, $Co_3O_4$ nanorods though p-type cannot act as a channel layer but avoid any hetero-junction formation with the SWCNTs, thus carrying the same charge (holes) throughout the device. The role of the Au nanoparticles and $Co_3O_4$ nanorods is to enhance the sensitivity by providing a greater surface to volume ratio. This helps in enhancing the sensitivity and is evident from our studies where the device response was minimal for the individual components. Whereas, for the synergistic combination of both the nanostructures the sensitivity has improved 2.5 fold. Thus, the novelty of the sensor lies in the synergistic combination of SWCNTs and Au loaded $Co_3O_4$ NRs, which are crucial in affording the high level of sensitivity towards cTnT by making use of biotin–streptavidin chemistry. Prior to performing analytical tests using the proposed biosensor, we carried out hybrid material characterization such as FE-SEM, TEM, and XRD. Further, we studied the effect of varying concentrations of gold during the process of synthesis and we set this at 1 mL of Au in the $Co_3O_4$ matrix. Furthermore, we conducted a quantitative analysis using the proposed biosensing strategy by increasing the concentration of troponin T up to 10 $\mu g\ mL^{-1}$ and observed an enhanced response.

## Experimental section

### Materials and reagents

Chloroauric acid ($HAuCl_4$), single-walled carbon nanotubes (SWCNTs), cobalt nitrate hexahydrate [$Co(NO_3)2{\cdot}6H_2O$], ammonium

fluoride (NH4F), urea, and streptavidin were all purchased from Sigma-Aldrich (USA). Highly doped n-type Si (n++) wafers were purchased from Si-Mat (Germany). All reagents were used as received without further purification. In this study, ultrapure water (18.2 MΩ cm) from a Milli-Q ultrapure system was used to prepare the aqueous solutions. The DNA aptamer (3′ biotinylated) protein was purchased from OTC Biotech (USA) and cTnT (the marker being tested) was purchased from ABCAM (UK).

### Synthesis of $Co_3O_4$ NRs

The $Co_3O_4$ NRs were synthesized using a facile hydrothermal method. In a typical procedure, 5 mmol of $Co(NO_3)_2$, 10 mmol of $NH_4F$, and 25 mmol of urea were dissolved in 70 mL of distilled water with vigorous stirring, which produced a pink-colored solution. This solution was then transferred to a Teflon-liner stainless steel autoclave with a volume capacity of 100 mL and heated in a programmable oven at 120 °C for 5 h. After the reaction was complete, the pink precipitate of cobalt hydroxide products was collected, washed, centrifuged with distilled water and ethanol alternately to remove unreacted ions, and then dried at 70 °C in an oven overnight. To make the final product crystalline and porous structures, the product was calcined at 350 °C for 2 h in the air to get black color $Co_3O_4$ NR powders.

### Synthesis of Au-decorated $Co_3O_4$ NR composites

To modify the surface of the $Co_3O_4$ NRs, we decorated Au nanoparticles (NPs) on them using a deposition–precipitation method at a low temperature. Initially, 0.01 g of $Co_3O_4$ NR powder was added to 25 mL of an aqueous solution of urea (0.42 M) and sonicated for complete mixing. Four aliquots of $HAuCl_4$ (0.01 M, 0.5–2 mL) solution were added drop by drop and stirred further for 10 min. Subsequently, the above mixture solutions were heated on a hotplate at 80 °C for 4 h with constant stirring. At the end of the reaction, the products were washed, centrifuged, and dried. Finally, the dried powder was calcined at 350 °C for 2 h to obtain Au-decorated $Co_3O_4$ NRs. According to the different amounts of $HauCl_4$, four materials with different Au-NP loading were obtained and are denoted as 0.5-Au/$Co_3O_4$ NRs, 1-Au/$Co_3O_4$ NRs, 1.5-Au/$Co_3O_4$ NRs and 2-Au/$Co_3O_4$ NRs, respectively. Fig. 1 illustrates the schematic of the synthesis process of pure $Co_3O_4$ NRs and Au-decorated $Co_3O_4$ NRs.

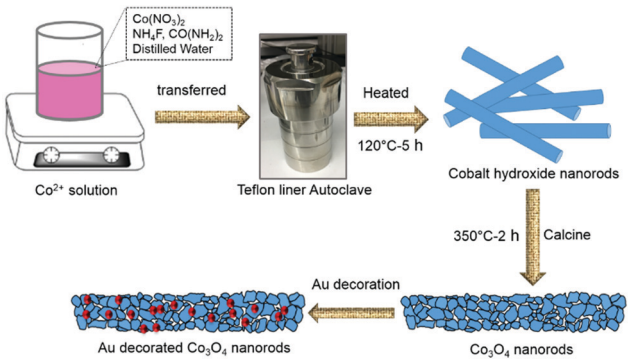


Fig. 1 Schematic illustration of the synthesis process of $Co_3O_4$ and Au-decorated $Co_3O_4$ NRs with the hydrothermal method using an autoclave and calcination approaches.

### Characterization of the nanomaterials

The morphologies of the as-synthesized $Co_3O_4$ NRs and Au-decorated $Co_3O_4$ NRs were characterized using a field-emission scanning electron microscope (FESEM; Zeiss) and transmission electron microscope (TEM; JEOL-JEM-2010) equipped with a charge-coupled device camera (operating voltage = 200 kV). The X-ray diffraction (XRD) patterns of the as-prepared materials were recorded on a Bruker D8 Phaser instrument with Cu-kα radiation ($k$ = 1.54178 Å). Gas sensing measurements were conducted using an in house developed setup at King Abdullah University of Science and Technology (KAUST), Saudi Arabia.

### Fabrication of transistor-based sensor devices and electrical measurements

We used highly doped 4-inch Si wafers (n++) to make the interdigitated electrode structures that essentially worked as the source and drain contacts of the transistor. Initially, single-sided polished Si wafers were cleaned using a Radio Corporation of America (RCA) process and were transferred immediately into an oxidation chamber for dry oxidation. The thermally grown oxide on top of the wafers was approximately 300 nm and deposited on both sides. The back oxide on the rough side was removed in buffered hydrofluoric acid (BHF). Subsequently, a lithography process was performed on top of the oxide layer using an AZ 5240 positive photoresist and a dark-field mask of interdigitated electrodes (IDE) was used to expose the sample to ultraviolet light at 80 mW. Furthermore, the wafer was developed in an AZ 700 developer for 1 min followed by being washed in deionized water. Finally, we deposited Ti/Au (10/200 nm) using sputtering in a vacuum at $2 \times 10^{-6}$ mBar. A lift off process was used to take off the Au and photoresist (sonication in acetone) to realize the source and drain electrodes. The distance between the electrodes was 100 μm and the width of the device was 24 100 μm. For the deposition, we started with 1 μL of SWCNT solution and drop-cast it on the IDE substrate (FET device), annealing it at 80 °C for 20 min to form the actual channel layer of the device. Then, 2.5 μL of $Co_3O_4$ NR solution decorated with Au nanoparticles was drop-cast on top of the SWCNTs in the channel region to form the receptor layer. Fig. 2 illustrates the fabrication process of the transistor-based sensor device using the as-synthesized $Co_3O_4$ NRs and Au-decorated $Co_3O_4$ NRs.

The full length troponin-T protein was purchased from ABCAM. The solutions of streptavidin and troponin-T were prepared in PBS (phosphate buffer saline, pH = 7.4) in 1× dilution using deionized distilled water from a Millipore water purification system. To perform the bio-functionalization during the experiment tiny amounts of streptavidin protein (~1 μL) were first attached to the surface followed by immobilization of the biotinylated DNA aptamer using the drop-casting method. Binding between the aptamer and streptavidin was facilitated using biotin–streptavidin chemistry. Finally, the target analyte cTnT

 

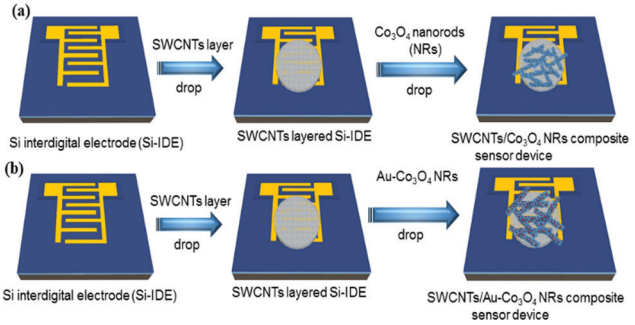


Fig. 2 Scheme illustrating the flow of the fabrication process (sensor devices) using (a) $Co_3O_4$ NRs and (b) Au-decorated $Co_3O_4$ NRs. The red spots on the NRs correspond to Au nanoparticles.

(~1 μL) was introduced into the device and the change in the electrical characteristics of the FET was measured and analyzed further. The above sequence was repeated for multiple runs for varying conditions, such as different gate bias voltages, thin-film thicknesses, and target concentrations.

## Results and discussion

### Morphological and structural characterization

$Co_3O_4$ NRs were synthesized using a one-step hydrothermal method (a detailed explanation was provided in the previous section). The morphology and structure of the as-synthesized $Co_3O_4$ NRs and Au–$Co_3O_4$ NRs obtained after calcination were examined using the FESEM. Fig. 3a and b display FESEM images of the hydrothermally synthesized $Co_3O_4$ nanoparticles, which clearly indicate that the products consisted of numerous rod-like structures. The obtained $Co_3O_4$ NRs had a diameter in the range of 100–200 nm and length up to 0.5–2 μm. Furthermore, it can be seen that the primary particles of which the $Co_3O_4$ NRs are composed were in the range of 40–60 nm. The TEM image in Fig. 3c further demonstrates the morphology of the $Co_3O_4$ NRs. It can be seen that the $Co_3O_4$ nanoparticles are aggregated during thermal treatment but still the $Co_3O_4$ NRs appears to be porous structures. The corresponding selected area electron diffraction (SAED) pattern shown in Fig. 3d further confirms the formation of polycrystalline structures of the $Co_3O_4$ NRs corresponding to the cubic $Co_3O_4$ phase. The $Co_3O_4$ porous NR structures were formed during the oxidation process of $Co(OH)_x(CO_3)_y{\cdot}nH_2O$ according to the following reaction:[33,34]

$$Co^{2+} + xF^- \rightarrow CoF_x^{(x-2)-} \quad (1)$$

$$NH_2CONH_2 + H_2O \rightarrow 2NH_3 + CO_2 \quad (2)$$

$$CO_2 + H_2O \rightarrow CO_3^{2-} + 2H^+ \quad (3)$$

$$NH_3{\cdot}H_2O \rightarrow NH_4^+ + OH^- \quad (4)$$

$$CoF_x^{(x-2)-} + 0.5(2-y)CO_3^{2-} + 2OH^- + H_2O \rightarrow Co(OH)_y(CO_3)_{0.5(2-y)}{\cdot}nH_2O + xF^- \quad (5)$$

$$3Co(OH)_y(CO_3)_{0.5(2-y)}{\cdot}nH_2O + 0.5O_2 \rightarrow Co_3O_4 + (3n+1.5y)H_2O + 1.5(2-y)CO_2. \quad (6)$$

XRD was conducted to confirm the structure and phase composition of the as-synthesized materials. Fig. 4 presents the XRD pattern of the as-synthesized $Co_3O_4$ NRs after being calcined at 350 °C. All diffraction peaks in the pattern can be assigned to the (220), (311), (222), (400), (422), (511), and (440) planes of cobalt tetroxide (JCPDS 74-1657). The narrow sharp peaks signify high crystallization of the $Co_3O_4$ nanostructures. However, no characteristic peaks of any other impurities can be observed, indicating that a high crystalline purity of $Co_3O_4$ was obtained through the hydrothermal process.

### Characterization of pure Au-decorated $Co_3O_4$ NRs

To compare the sensing performance, Au NPs were deposited on the as-synthesized $Co_3O_4$ NRs by a deposition–calcination method as described in the synthesis procedure. Fig. 5a is the FESEM image of 1 mL Au-decorated $Co_3O_4$ NRs.

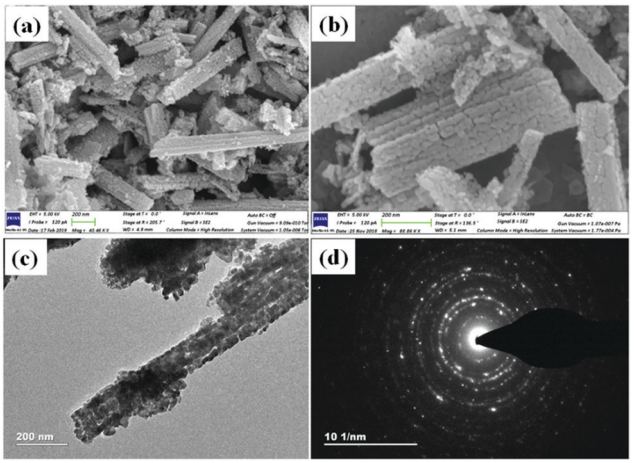


Fig. 3 FESEM of $Co_3O_4$ NRs at (a) 43 K× magnitude and (b) 88 K× magnitude highlighting the pores and TEM (c) images (prepared as per the synthesis process in the Experimental section); (d) selected area diffraction (SAED) pattern of polycrystalline $Co_3O_4$ structures.

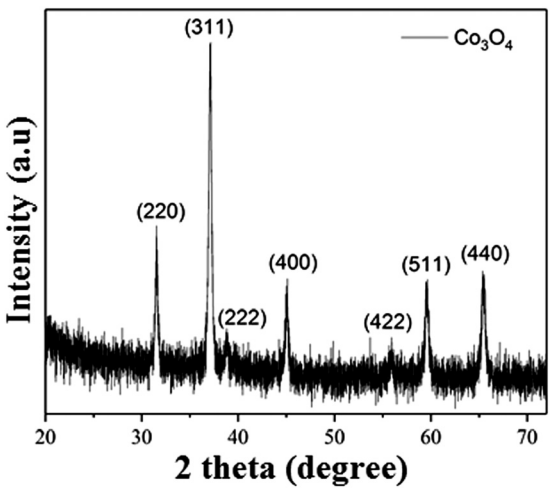


Fig. 4 XRD pattern of the hydrothermally synthesized $Co_3O_4$ NRs calcined at 350 °C for 2 h.

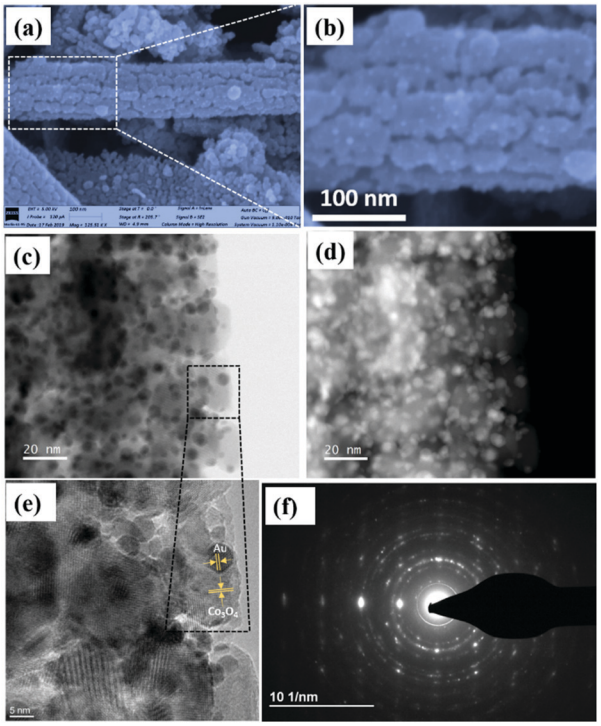


Fig. 5 (a and b) FESEM images, (c) TEM image, (d) HAADF image, (e) HR-TEM image recorded from the black dotted area of image (d), and (f) selected area diffraction (SAED) pattern of the 1-Au/$Co_3O_4$ NR sample.

From these figures, it is evident that small Au NPs were deposited throughout the $Co_3O_4$ NR surface after Au nanoparticles were decorated on the $Co_3O_4$ NR surface, and are distributed well across the whole surface.

From Fig. 5b, numerous tiny white spherical particles (representing Au nanoparticles) were assembled on the $Co_3O_4$ NR surface, which had an average size in the range of 3–5 nm.

Fig. 5d shows the HAADF-STEM image of the 1-Au-loaded $Co_3O_4$ NRs, which further confirmed the deposition of Au NPs. Fig. 5e shows the HR-TEM image of the 1-Au-loaded $Co_3O_4$ NRs, which was recorded from the black dotted box as shown in Fig. 5c. It clearly shows the lattice fringes of Au and $Co_3O_4$, respectively.

Also, Fig. 5f shows the SAED pattern of the 1-Au-loaded $Co_3O_4$ NRs indicating the polycrystalline nature of the prepared materials. Fig. 6(a–d) shows the morphologies of as prepared different variations of Au deposited $Co_3O_4$ NRs depending on the amount of $HAuCl_4$ from 0.5 to 2 mL. It can be seen that after increasing the loading amount of $HAuCl_4$ to 1.5 mL, the small Au NPs were fully dispersed throughout the $Co_3O_4$ NR surface. After further increasing the loading amount of $HAuCl_4$ to 2 mL, the size of the Au NPs increased and they agglomerated on the surface of the $Co_3O_4$ NRs.

### Sensing measurements

We extracted the transient response of the CNT-based FET device over a period of 5 min (optimized) at multiple stages. The corresponding SEM images of the device are shown in Fig. 7, where we depicted the device deposited with SWCNTs

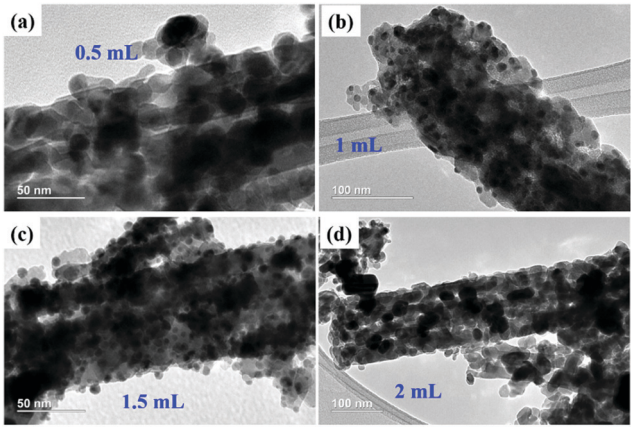


Fig. 6 TEM images of (a) 0.5-Au/$Co_3O_4$ NRs, (b) 1-Au/$Co_3O_4$ NRs, (c) 1.5-Au/$Co_3O_4$ NRs, and (d) 2-Au/$Co_3O_4$ NRs.

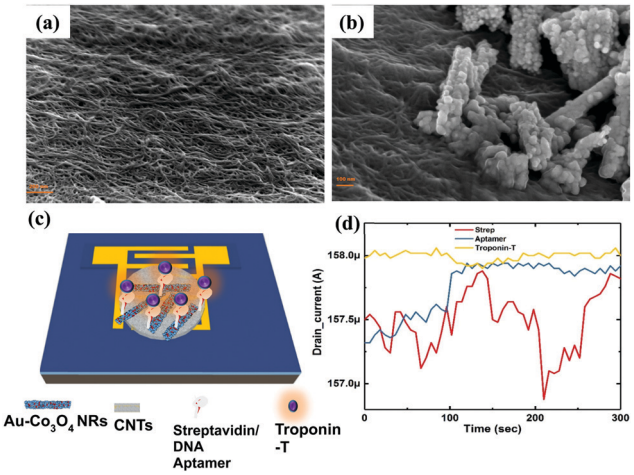


Fig. 7 SEM image of (a) SWCNTs on the Si/$SiO_2$ substrate, (b) Au/$Co_3O_4$ NRs on top of the SWCNTs, (c) the FET with immobilized bilayer-2, and (d) the transient response (drain current) of the CNT device alone at multiple stages of functionalization.

alone (Fig. 7a) and SWCNT/Au–$Co_3O_4$ NRs (Fig. 7b) separately. Further analysis was conducted as per the data generated from bare devices and the targeted bioanalyte bound devices. An interesting observation was made toward the end, and the results were in agreement with our previous study on the ZnO platform.[24] Initially, control experiments were performed to detect the target analyte with SWCNTs alone, as shown in Fig. 7d.

We did not observe any change in the drain current of the device after functionalization of the surface and after introducing cTnT onto the functionalized surface. Next, the $Co_3O_4$ NRs were introduced on top of the SWCNTs as a receptor layer, essentially forming a complete bilayer, and the immobilization steps were performed accordingly. In a relevant study, CNTs were used as a channel material along with receptor layers in a FET configuration with a primary focus on chemical sensing.[35] Furthermore, in some reports, modified CNTs have been directly used as a channel/sensing layer. For example, Gomes-Filho *et al.*

 

reported the use of carboxylated CNTs (C-CNTs) for the detection of cTnT,[36] where the amine group in polyethyleneimine allowed covalent binding between antibodies and COOH-CNT. Similarly, Barbara *et al.* reported using $NH_2$-CNT on top of a PET sheet for the detection of cTnT, where the carboxylic group was present on the anti-cTnT antibodies.[37]

Thus, for transduction to occur, the presence of a binding group is essential for successful detection. Thus we employed another approach with SWCNT/$Co_3O_4$ (bilayer-1) and immobilized both streptavidin and the DNA aptamer on it, and then it was tested for cTnT. We observed a change of approximately 1.5% in the drain current from the baseline, as shown in Fig. 8a. This slight change could be attributed to the presence of $Co_3O_4$ NRs. Similarly, as shown in Fig. 7c, another bilayer consisting of Au nanoparticle-embedded $Co_3O_4$ NRs as a receptor layer was coated on the top of the channel layer of the SWCNTs, forming a combination of SWCNT/Au-$Co_3O_4$ (bilayer-2).

This was again immobilized as per the standard process and tested for the cTnT analyte. Here, we observed a maximum change of more than 4.2% in terms of the drain current change from the baseline, as shown in Fig. 8b. Thus, we recorded an increase in sensitivity of more than 250% with the new receptor layer embedded with Au nanoparticles. A DNA aptamer is well known to engender a negative charge in the surface of semiconductors, and thus its functionalization on the p-type channel layer accumulates electrons and reduces the channel current. Furthermore, the interaction between cTnT and the immobilized DNA aptamer leads to a conformational change in the secondary structure of the aptamer, which brings in a more negative charge to the channel layer. A plausible mechanism for the improved sensitivity (in the case of the Au-decorated $Co_3O_4$ NRs) could be the synergistic effect of Au nanoparticles and $Co_3O_4$ NRs in the channel layer. Here, the Au NPs help in the increased adsorption of negatively charged DNA molecules on the surface of the $Co_3O_4$ NRs. Therefore, holes become depleted in the channel because of the enhanced interaction between Au binding sites and secondary structures, eventually leading to a reduced drain current. The Au nanoparticles also play a crucial role in immobilizing biomolecules and enhancing the response signal owing to their high surface area, excellent conductivity and high catalytic properties. Au's high workfunction aids the transfer of electrons from $Co_3O_4$ to Au while avoiding any direct charge interaction with the channel layer (SWCNTs). As it can be seen from Fig. 8b, after the immobilization of the DNA aptamer on Au–$Co_3O_4$ the drain current reduces (unlike Fig. 8a), which may be due to the difference in work function between gold (5.1–5.47 eV) and $Co_3O_4$ (4.5 eV). Thereafter, a further decrease in current is observed after introducing the target cTnT on the Au/$Co_3O_4$/CNT composite.

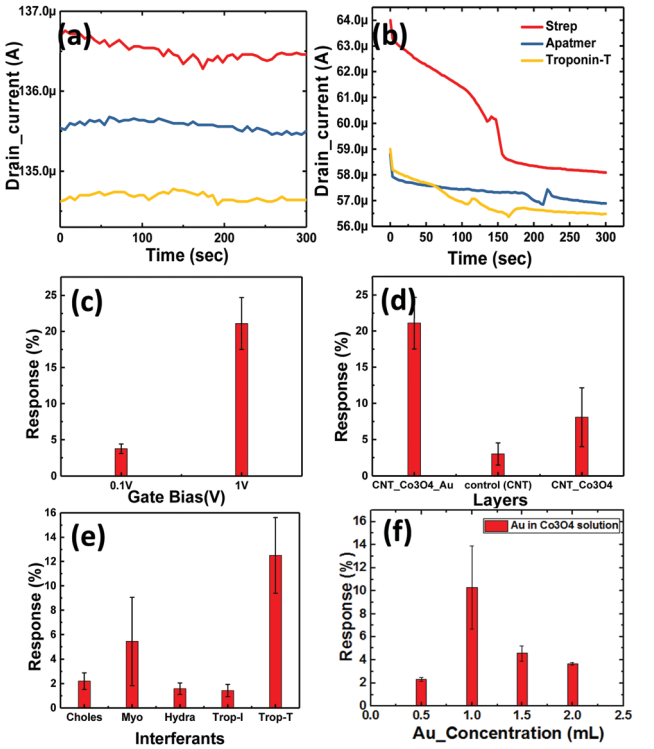


Fig. 8 Transient response (drain current) of the device with (a) $Co_3O_4$ NRs and (b) Au–$Co_3O_4$ NRs on the top CNT channel layer. Bar graphs comparing the response variation with (c) different gate biases (0.1 V and 1 V) and (d) different base layers corresponding to Au–$Co_3O_4$ NR/CNT, CNTs and $Co_3O_4$ NR/CNT. (e) Selectivity study with different biological interferents. (f) The response of the sensor with multiple concentrations of gold loading in the $Co_3O_4$ NR system.

The bar graph in Fig. 8c indicates the dependence of the drain current on the gate bias. Initial runs to test the performance of the novel biosensor were performed with the lowest possible bias voltage of 0.1 V on the drain and gate terminals when the source was grounded, whereas the actual measurements were performed with the drain fixed at 0.1 V and the gate bias increased to 1 V (max in the current device configuration). For an order of magnitude change in the gate voltage, we observed a 5.4-times change in the drain current sensitivity (S) with bilayer-2. Here, we observed that the charge transfer from the DNA aptamer to $Co_3O_4$ resulted in reduced conduction of the device. This was because of the presence of a negative phosphate group in the DNA, which contributed to the electron doping in both combinations (bilayer-1 and -2). However, the further decrease in drain current was attributed to the presence of Au nanoparticles, because they efficiently catalyzed the oxidation and the corresponding response obtained with different bilayers can be seen in Fig. 8d. The response time of the device was 2 min, and 50% response was achieved in 15 s. Once the platform was ready, the entire process of immobilization and testing could be performed in 10 min. In addition, the devices can be reused for multiple runs of cTnT detection or any similar marker for other biosensing activities. Selectivity studies have been performed with different biomarkers like cholesterol (choles), myoglobin (myo), hydrazine (hydra) and troponin-I (cTnI) as shown in Fig. 8e. We considered biomarkers like myo and cTnI based on previous reports for the AMI condition and the other biomarkers are irrelevant to AMI. Our device was highly selective towards cTnT detection and responded with minimal intensity to the other

biomarkers mentioned above. However, the response to myoglobin was 50% of that of cTnT which can be abbreviated to the myoglobin response lagging to cTnT where the latter immediately spikes in the blood after the onset of AMI and settles down gradually.

### Effect of the Au concentration used for the decoration of $Co_3O_4$ NRs

Here, we also made measurements with multiple $Co_3O_4$ NRs loaded with different concentrations of Au nanoparticles (as mentioned in Section 2). The obtained results are shown in Fig. 8f and clearly depict the influence of the amount of Au NPs in the system. We further observed that the deviation in the response to troponin-T is high for the optimized concentration of Au on the $Co_3O_4$ NRs and also realized that the response degrades with heavier loading. The 1.5-Au/$Co_3O_4$ NR and 2-Au/$Co_3O_4$ NR devices showed relatively lower responses and the plausible explanation could be the aggregation and large particle formation of Au NPs, which lowers the catalytic activity. Also, the lower availability of catalytic surface sites of $Co_3O_4$ NRs in the 1.5-Au/$Co_3O_4$ NR and 2-Au/$Co_3O_4$ NR samples also might be another reason for the lower responses. Thus, we conclude that 1 mL of Au in the $Co_3O_4$ NR solution during the synthesis yields good results and is an optimum value for the efficient response of the device.

The measurements in Fig. 9 were performed under continuous gate and drain biases, unlike in Fig. 6 and 7, where both the gate and drain biases were switched off before every step of the protocol. The motive behind such a measurement was to understand the influence of bias stress during the execution of the protocol. We observed no differences in the readings of drain current for switching and continuous gate biases. Furthermore, the response clearly distinguished between three different concentrations, low (approx. 1 μg $mL^{-1}$), medium (5 μg $mL^{-1}$) and high concentration immobilization (approx. 10 μg $mL^{-1}$), of the target cTnT. From Fig. 9a, it is evident that the response of the drain current decreases as the concentration of cTnT increases, and high concentrations of the DNA aptamer and cTnT had similar changes, as observed in Fig. 9b.

We performed sensitivity studies on the device with multiple concentrations of troponin-T as shown in Fig. 9c. These measurements belong to the final step of the entire process of sensing activity and are presented on a log scale ($x$-axis). The measured LOD of the device is 0.1 μg $mL^{-1}$ with the maximum concentration being 10 μg $mL^{-1}$. Fig. 9c illustrates the variation of the response with increasing concentration of the cTnT analyte covering the whole range. The inset in Fig. 9c corresponds to the linear response range for cTnT and was crucial in determining the LOD. We observed negligible changes in the drain current characteristics for a concentration below the LOD as the optimized receptor concentration was not enough to generate adequate signal. In our previous work,[24] we took the approach of a TFT with ZnO layers, where the response depends completely on the surface interaction. In the current study, as stated earlier, our target was to reduce the sensor element size to analyte level to improve the sensitivity and thus we carried our experiments with nanoparticles and nanorods that essentially improve the overall surface area for interaction.

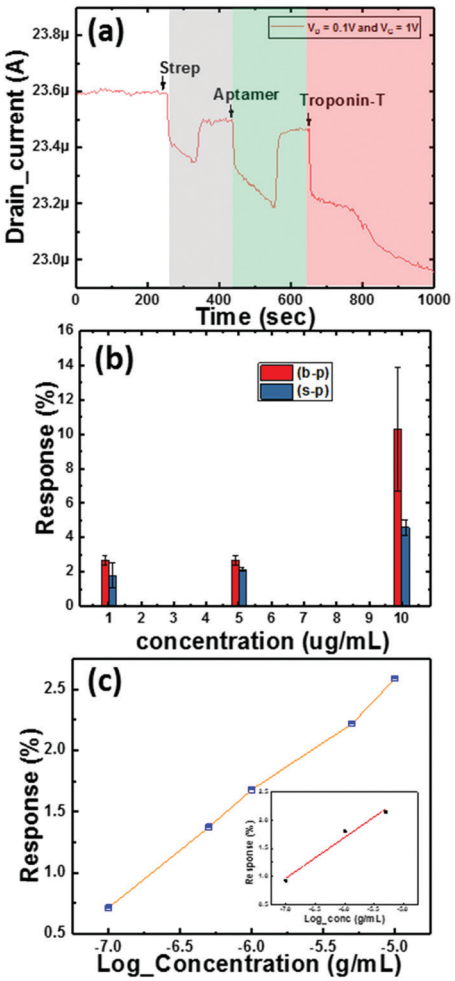


Fig. 9 (a) Transient response (drain current) of the device with low concentration (approx. 1 μg $mL^{-1}$); (b) bar graph of responses at 3 different concentrations of troponin-T (1, 5 and 10 μg $mL^{-1}$), and for different baselines; and (c) the response of the devices for different concentrations of analyte to identify the LOD (immediately after immobilization), the inset shows the linearity curve.

Studies were conducted on three channel layers of the FET, SWCNTs (control), bilayer-1, and bilayer-2, to observe the responses to cTnT. We used $Co_3O_4$ NRs, a p-type material, for the first time and concomitantly observed an increase in the device sensitivity with Au NP decoration. Morphological studies conducted using FESEM and TEM confirmed the nanostructures and presence of Au nanoparticles. Similarly, electrical characterization helped in understanding the performance of the device through the drain current to detect the AMI condition. Table 1 classifies the AMI detection capability using troponins with different FET platforms. Both cTnI and cTnT have been considered for the comparison. Our Au-decorated $Co_3O_4$ NR based FET showed a high response (250%) with a sample volume of 1 μL (0.1 μg $mL^{-1}$) of target analyte cTnT.

Further, we observed that the FETs developed with complex CMOS technology performed well in terms of the LOD. Thus we consider that our device has limitations in detecting lower concentrations of cTnT but we fared well in using lower sample

 

Table 1 Comparison among different FET platforms

| Target analyte | Device | LOD (μg mL$^{-1}$) | Sensitivity | Sample volume (μL) | Selectivity |
|---|---|---|---|---|---|
| cTnT[25] | ZnO FET | 10 | 0.15 μA | 10 | No |
| cTnI[38] | $SnO_2$ FET | 0.02 | NA | 30 | No |
| cTnT[39] | SiNW FET | 0.01 | 25% | NA | Yes |
| cTnI[3] | SWCNT_Au FET | $1.00 \times 10^{-6}$ | 14% | NA | No |
| cTnI[40] | FET | 0.02 | 6.40% | 50 | No |
| cTnT [our work][41] | SWCNT/Au–$Co_3O_4$ FET | 0.1 | 0.5 μA (250%) | 1 | Yes |

volume and selectivity. Among five different target analytes, the Au-decorated $Co_3O_4$ NR based FET was highly sensitive for troponin-T alone. Our device capability is in the range of physiological concentration (<14 ng L$^{-1}$), but still higher sensitivities can be achieved through controlled deposition techniques during the immobilization and identification phases. In addition, implementation of processes like nanoimprint lithography kinds of techniques for the proposed material combination might help in improving the sensitivity and achieving the desired LODs. In addition, tests were conducted with liquid drops one on top of the other to check the compatibility of the Au–$Co_3O_4$ in multielectrode probe systems like screen printed electrodes (PalmSens),[41] where the solutions can be contained. The results confirmed that a test platform co-existing with PalmSens can be utilized to build a hybrid system. This can eventually be helpful in elevating the current platform to a system embedded with pattern recognition with improved detection accuracy.

## Conclusions

Here, we successfully demonstrated a versatile and robust SWCNT FET device modified with nanostructures and an aptamer to detect cTnT. Bilayer-2 proved to be the most sensitive layer because of the synergistic combination of Au nanoparticles decorated on top of the $Co_3O_4$ NRs. In addition, this was the first time that $Co_3O_4$ NRs, a p-type semiconductor, were used in the detection of the AMI condition through cTnT detection. Transient analysis was performed during surface immobilization and testing to observe the changes induced in the drain current (ID). We also evaluated the performance of the sensor platform at three different concentrations (1, 5 and 10 μg mL$^{-1}$), and significant changes were observed. The LOD of the sensor was 0.1 μg mL$^{-1}$ with a sample volume of 1 μL and the sensitivity of the proposed sensor was 0.5 μA μg$^{-1}$ mL$^{-1}$, which increased by approximately 250% compared with pure $Co_3O_4$ NRs. In addition, the drain current sensitivity ratio at different gate biases (S(0.1)/S(1)) was found to be 5.4. As compared to other devices the limitation in our device is its LOD capability and this can be improved by altering the fabrication process in the future course of this work. The proposed DNA aptamer-based sensor system is novel and can be developed into an integrated and high-throughput system.

## Conflicts of interest

The authors declare that they have no competing interests.

## Acknowledgements

We thank Ulrich Buttner of Microfluidic Lab, part of the Nanofabrication Core Lab, King Abdullah University of Science and Technology (KAUST), Saudi Arabia for providing his assistance in the project.

## Notes and references

1 J. E. Adams, K. B. Schechtman, Y. Landt, J. H. Ladenson and A. S. Jaffe, *Clin. Chem.*, 1994, **40**, 1291–1295.
2 H. A. Katus, A. Remppis, F. J. Neumann, T. Scheffold, K. W. Diederich, G. Vinar, A. Noe, G. Matern and W. Kuebler, *Circulation*, 1991, **83**, 902–912.
3 R. V. Sharma, N. K. Puri, R. K. Singh, A. M. Biradar and A. Mulchanadani, *Appl. Phys. Lett.*, 2013, **103**, 203703.
4 V. V. Shumyantseva, L. V. Sigolaeva, L. E. Agafonova, T. V. Bulko, D. V. Pergushov, F. H. Schacher and A. I. Archakov, *J. Mater. Chem. B*, 2015, **3**, 5467–5477.
5 D. K. Agarwal, A. Prasad, M. Vinchurkar, S. Gandhi, D. Prabhakar, S. Mukherji and V. R. Rao, *Appl. Nanosci.*, 2018, **8**, 1031–1042.
6 X. Zhang, H. Lv, Y. Li, C. Zhang, P. Wang, Q. Liu, B. Ai, Z. Xu and Z. Zhao, *J. Mater. Chem. B*, 2019, **7**, 1460–1468.
7 S. Sivashankar, C. Sapsanis, U. Buttner and K. N. Salama, *Electron. Lett.*, 2015, **51**, 1746–1748.
8 I. Lee, X. Luo, J. Huang, X. T. Cui and M. Yun, *Biosensors*, 2012, **2**, 205–220.
9 G. Cabral-Miranda, E. Yamashiro-Kanashiro, M. Gidlund and M. G. F. Sales, *J. Mater. Chem. B*, 2014, **2**, 477–484.
10 S. G. Surya, S. Nag, N. M. Duragkar, D. Agarwal, G. Chatterjee, S. Gandhi, S. Patil, D. K. Sharma and V. R. Rao, *J. Low Power Electron.*, 2012, **8**, 346–352.
11 N. Akhtar, M. Y. Emran, M. A. Shenashen, H. Khalifa, T. Osaka, A. Faheem, T. Homma, H. Kawarada and S. A. El-Safty, *J. Mater. Chem. B*, 2017, **5**, 7985–7996.
12 M. Li, H. X. Tang and M. L. Roukes, *Nat. Nanotechnol.*, 2007, **2**, 114.
13 T. Hirao, M. Furuta, T. Hiramatsu, T. Matsuda, C. Li, H. Furuta, H. Hokari, M. Yoshida, H. Ishii and M. Kakegawa, *IEEE Trans. Electron Devices*, 2008, **55**, 3136–3142.
14 A. C. M. De Moraes and L. T. Kubota, *Chemosensors*, 2016, **4**, 20.
15 Y.-W. Huang, C.-S. Wu, C.-K. Chuang, S.-T. Pang, T.-M. Pan, Y.-S. Yang and F.-H. Ko, *Anal. Chem.*, 2013, **85**, 7912–7918.
16 W. Peng, S. Qu, G. Cong and Z. Wang, *Cryst. Growth Des.*, 2006, **6**, 1518–1522.

17 D. Sarkar, W. Liu, X. Xie, A. C. Anselmo, S. Mitragotri and K. Banerjee, *ACS Nano*, 2014, **8**, 3992–4003.
18 Y.-M. Chu, C.-C. Lin, H.-C. Chang, C. Li and C. Guo, *Biosens. Bioelectron.*, 2011, **26**, 2334–2340.
19 K. Kim, C. Park, D. Kwon, D. Kim, M. Meyyappan, S. Jeon and J.-S. Lee, *Biosens. Bioelectron.*, 2016, **77**, 695–701.
20 S. Pineda, Z. J. Han and K. Ostrikov, *Materials*, 2014, **7**, 4896–4929.
21 X. Tong, E. Ashalley, F. Lin, H. Li and Z. M. Wang, *Nano-Micro Lett.*, 2015, **7**, 203–218.
22 S. K. Arya, S. Saha, J. E. Ramirez-Vick, V. Gupta, S. Bhansali and S. P. Singh, *Anal. Chim. Acta*, 2012, **737**, 1–21.
23 Q. Liu, N. Aroonyadet, Y. Song, X. Wang, X. Cao, Y. Liu, S. Cong, F. Wu, M. E. Thompson and C. Zhou, *ACS Nano*, 2016, **10**, 10117–10125.
24 M. F. M. Fathil, M. K. M. Arshad, M. N. M. Nuzaihan, S. C. B. Gopinath, A. R. Ruslinda and U. Hashim, *IOP Conf. Ser.: Mater. Sci. Eng.*, 2018, **318**, 012031.
25 D. K. Agarwal, M. Kandpal and S. G. Surya, *Appl. Surf. Sci.*, 2019, **466**, 874–881.
26 S. Elhag, Z. Ibupoto, O. Nour and M. Willander, *Materials*, 2015, **8**, 149–161.
27 X. Luo, A. Morrin, A. J. Killard and M. R. Smyth, *Electroanalysis*, 2006, **18**, 319–326.
28 R. Ahmad, T. Bedük, S. M. Majhi and K. N. Salama, *Sens. Actuators, B*, 2019, **286**, 139–147.
29 R. Ahmad, O. S. Wolfbeis, Y.-B. Hahn, H. N. Alshareef, L. Torsi and K. N. Salama, *Mater. Today Commun.*, 2018, **17**, 289–321.
30 D. T. Thompson, *Nano Today*, 2007, **2**, 40–43.
31 M. Gautam and A. H. Jayatissa, *Solid-State Electron.*, 2012, **78**, 159–165.
32 S. Zeng, K.-T. Yong, I. Roy, X.-Q. Dinh, X. Yu and F. Luan, *Plasmonics*, 2011, **6**, 491.
33 H. Nguyen and S. A. El-Safty, *J. Phys. Chem. C*, 2011, **115**, 8466–8474.
34 X.-h. Xia, J.-p. Tu, Y.-q. Zhang, Y.-j. Mai, X.-l. Wang, C.-d. Gu and X.-b. Zhao, *RSC Adv.*, 2012, **2**, 1835–1841.
35 B.-C. Kang, B.-S. Park and T.-J. Ha, *Appl. Surf. Sci.*, 2019, **470**, 13–18.
36 S. Gomes-Filho, A. Dias, M. Silva, B. Silva and R. Dutra, *Microchem. J.*, 2013, **109**, 10–15.
37 B. V. Silva, I. T. Cavalcanti, M. M. Silva and R. F. Dutra, *Talanta*, 2013, **117**, 431–437.
38 Y. Cheng, K.-S. Chen, N. L. Meyer, J. Yuan, L. S. Hirst, P. B. Chase and P. Xiong, *Biosens. Bioelectron.*, 2011, **26**, 4538–4544.
39 G. J. Zhang, Z. H. H. Luo, M. J. Huang, G. K. I. Tay, E. J. A. Lim and Y. Chen, *Int. Electron Devices Meet.*, 2009, 563–566.
40 T. Kong, R. G. Su, B. B. Zhang, Q. Zhang and G. S. Cheng, *Biosens. Bioelectron.*, 2012, **34**, 267–272.
41 M. Čadková, V. Dvořáková, R. Metelka, Z. Bílková and L. Korecká, *Electrochem. Commun.*, 2015, **59**, 1–4.

 